Integrated Magnetics Design for a Three-Phase Differential-Mode Rectifier

Moien Mohamadi, *Student Member, IEEE*, Sudip Kumar Mazumder, *Fellow, IEEE*, and Nikhil Kumar, *Student Member, IEEE*

***Abstract*—In this article, the design methodology of integrated magnetics (IM) for a three-phase differential-mode Ĉuk rectifier (DMCR) is outlined. The design and optimization of the IM are so achieved such that the inductor current ripple, total harmonic distortion of the input current, and magnetics loss are optimized without compromising the stability of the DMCR. The optimization and design of the IM are conducted using the Maxwell and SaberRD software tools, and subsequently, the results are compared with a plurality of other IM structures for performance comparison. Finally, the experimental hardware for the DMCR comprising the optimized IM is fabricated to validate its performance and compare it with a DMCR fabricated solely using discrete magnetics.**

***Index Terms*—Differential mode, efficiency, integrated magnetics (IM), loss, rectifier, ripple, stability, total harmonic distortion (THD), winding.**

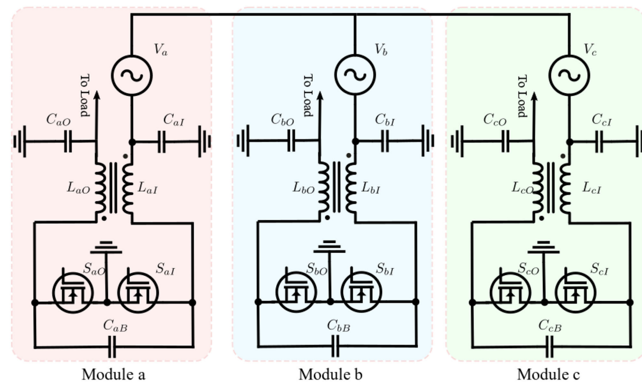

Fig. 1. IM-based three-phase DMCR comprising three converter modules and three IM devices (inductors). A DM-based realization requires six DM devices.

I. Introduction

POWER converters often require a plurality of magnetic components with functionalities ranging from filtering to galvanic isolation. Such magnetic components may be combined to form integrated magnetics (IM) that enable a reduction in the number of magnetic components [1], [2] to reducing current/voltage ripples [3]. Since its conception, IM has been used for a plurality of power-electronic-system (PES) applications and functions [4]–[20].

In such applications, regardless of their benefits, the IM design has a plurality of challenges to overcome. Such challenges encompass achieving uniformity in magnetic flux distribution, intermodulations among voltages or currents of transformers or inductors sharing the same magnetic core, enhanced transformer leakage inductance, winding placement, and tuning the coupling factor [14], [15], [18], [19], [21]–[23].

Notwithstanding, there are some issues that have received limited attention in the literature of IM. To begin with, since an IM changes the steady-state and transient dynamics of a PES, the stability margin and response of the latter should be carefully taken into consideration [14], [21], [22]. Small- and large-signal implications of IM should also be embedded in the PES design to realize optimal design-dynamics tradeoff depending on the application. Another implication of IM is on the power quality of the PES that needs a closer look. After all, the magnetic coupling introduces additional impedance in the circuit. This changes the power-decoupling dynamics and affects the power quality of the PES.

Following these motivations, in this article, an IM is proposed for a three-phase differential-mode Ĉuk rectifier (DMCR) [outlined in [24] with discrete magnetics (DM)], comprising three Ĉuk converter modules connected in a differential-mode configuration. The IM-based DMCR is shown in Fig. 1. It integrates the source- (ac-side) and load-side (dc-side) inductors of the Ĉuk converter to optimize flux cancelation, efficiency, dynamics, and power quality of the DMCR. The impact of the coupling factor of the IM on the performance and operation of the DMCR is initially investigated to determine the needed optimum coupling for the IM. Subsequently, the effects of different physical realizations of the IM are analyzed in relation to magnetics performance, which in turn, affect the performance of the DMCR.

This article is different from the earlier work by Ĉuk in [3] in the following respects. First, the article is focused on ac/dc and not dc/dc conversion. Second, our focus is on using the coupling factor of the IM as a control variable to achieve a desired input total harmonic distortion (THD) and DMCR stability while coachieving higher efficiency. This article is also different from the article presented in [18] regarding the same

Manuscript received July 14, 2020; revised January 31, 2021; accepted March 13, 2021. Date of publication March 17, 2021; date of current version June 1, 2021. This work was supported by the Advanced Research Projects Agency-Energy, U.S. Department of Energy in the CIRCUITS program monitored by Dr. Isik Kizilyalli under Award No. DE-AR0000903. Recommended for publication by Associate Editor F. Luo. *(Corresponding author: Sudip Kumar Mazumder.)*

The authors are with the Department of Electrical and Computer Engineering, University of Illinois at Chicago, Chicago, IL 60607 USA (e-mail: mmoham65@uic.edu; mazumder@uic.edu; nkumar22@uic.edu).

Color versions of one or more figures in this article are available at https://doi.org/10.1109/TPEL.2021.3066506.
Digital Object Identifier 10.1109/TPEL.2021.3066506

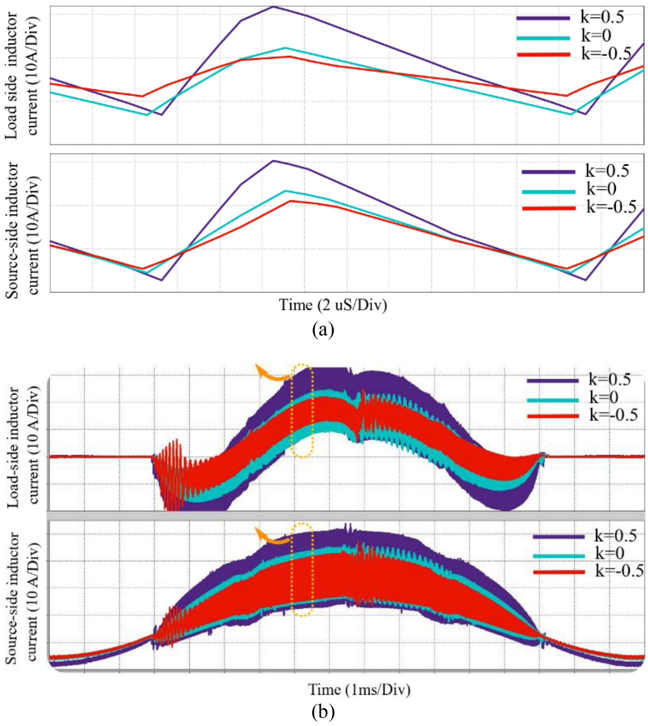

Fig. 2. (a) High- and (b) low-frequency waveforms for the load- and source-side magnetics of the DMCR. The top and bottom traces in (a) and (b) correspond to the load- and source-side waveforms, respectively.

two performance–parametric issues aside from the fact that this article focuses on a three-phase PES with nonlinear gain as against a single-phase PES with linear gain outlined in [18]. Furthermore, unlike the article presented in [18], DMCR operates with a discontinuous modulation scheme (DMS). Finally, this article is also different from the article presented in [24] and [25], which, even though focused on three-phase conversion, do not involve IM.

The rest of this article is organized as follows. In Section II, the impact of magnetic integration of the inductors on the stability, power quality, and efficiency of the DMCR is analyzed. In Section III, several computer-aided designs (CAD) of the IM are pursued to achieve a design with optimal performance. In Section IV, the experimental validation of the IM for the DMCR is presented and the results are compared with that obtained using DM. Subsequently, IM designs with four different coupling factors were tested and compared. Finally, in Section V, the conclusion of this article and its implications are outlined.

II. Impact of IM Coupling on the DMCR

The IM-based DMCR is illustrated in Fig. 1. The source- and load-side inductor currents of the DMCR, operating with DMS [24], are shown in Fig. 2. The source-side inductor of the DMCR converter module is subjected to low-frequency sinusoidal and high-frequency switching currents, while the load-side inductor is subjected to low- and high-frequency currents but with an added dc bias.

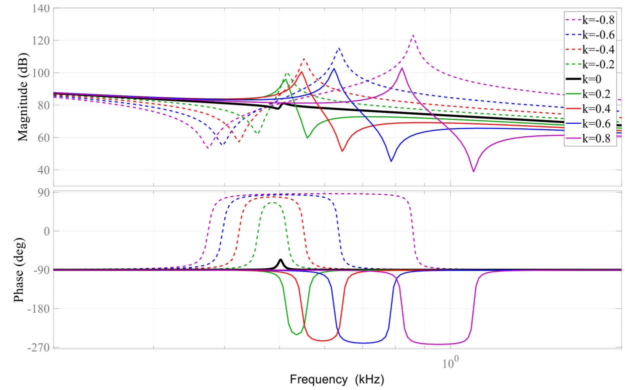

Fig. 3. Impact of the IM coupling factor on the open-loop response of the duty-cycle-to-input-current transfer function of one of the DMCR modules.

A. Stability

One of the objectives of the proposed IM is to achieve a reasonable stability margin, while flux cancelation and power quality are ensured. The implementation of magnetic coupling between the source- and load-side magnetics results in a feed-forward path from the input to the output. This added path may affect the stability of the DMCR.

The open-loop duty-cycle-to-input-current frequency response of one of the modules of the DMCR is shown in Fig. 3 where that part of the frequency spectrum, which is affected by the IM, is primarily demonstrated. It shows that the amplitudes of the resonance peaks increase with increasing coupling factor. This resonance frequency in the DMCR, if excited by an input, cause spikes or oscillations. To control these oscillations, either damping needs to be introduced, which will result in losses [26], or the coupling of the IM should be controlled.

The bandwidth of the open-loop transfer function is another important factor for the DMCR application. To perform power-factor correction without complicated control, the bandwidth of the open-loop transfer function needs to be high enough to carry out the current control and input-voltage tracking. The bandwidth of the DMCR with varying coupling factor for the IM is captured in Fig. 4. Operating the DMCR with the duty cycle close to unity yields a drop in the bandwidth. Therefore, a high coupling factor needs to be avoided.

B. Total Harmonic Distortion

The high- and low-frequency current pathways for the IM-based DMCR are shown in Fig. 5. The amplitude of the nth harmonic of the high-frequency current ripple (Δi_L) is expressed as follows:

$$I_h\ (n) = \left(\frac{2\Delta i_L}{\pi^2}\right)\left(\frac{1}{(2n-1)^2}\right)\cos\left(\frac{2\pi\,(2n-1)\,t}{T}\right). \tag{1}$$

Improving the current ripple, which can be controlled by varying the coupling factor (k) of the IM, and as demonstrated in Fig. 6, improves the DMCR's input-current THD, as given

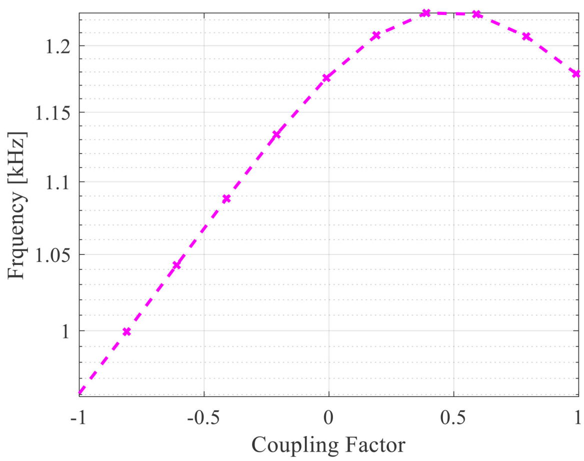

Fig. 4. Bandwidth of the open-loop duty-cycle-to-input-current transfer function for the IM-based DMCR with varying coupling factor.

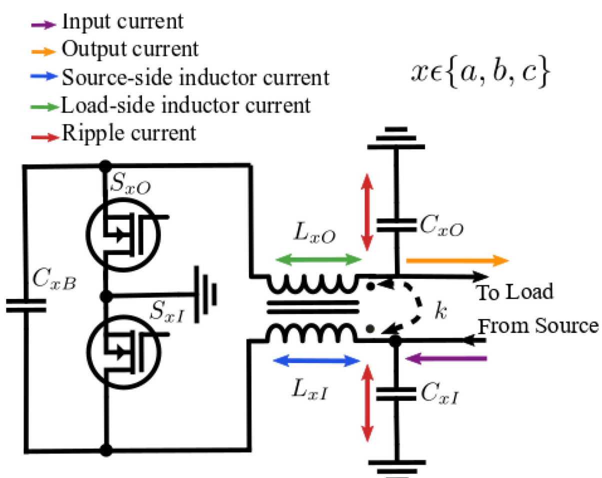

Fig. 5. Current pathways in the IM-based DMCR module.

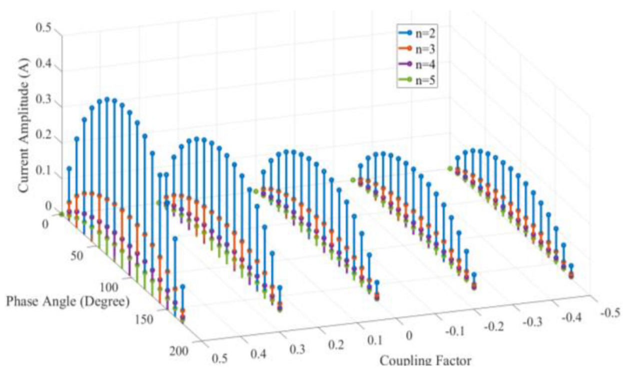

Fig. 6. Impact of the IM coupling factor (k) on the amplitude of the harmonic current over the low-frequency (60 Hz) half-a-line cycle.

by $\mathrm{THD}_I = \sqrt{\sum_{n\neq 1} I_h(n)^2}/I_f$, where I_f is the fundamental components of input current. Implementing effective ripple mitigation in the IM yields an adequately effective input inductance protecting the ac source from high-frequency harmonics resulting in reduced need for the line inductance.

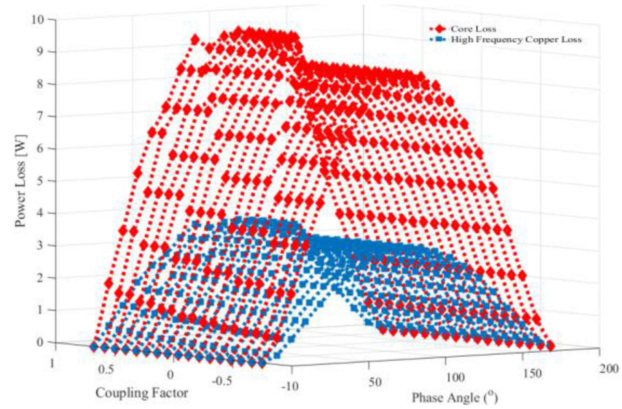

Fig. 7. High-frequency core and copper losses of the IM for varying coupling factor over half-a-line-cycle operation of the DMCR.

C. *Efficiency*

The core loss in the magnetic devices is dependent on the frequency of flux cycle, dc current level, and ripple magnitude [27], [28]. For the DMCR, the load-bias current level and the ripple change over a line cycle. Using the IM, via ripple cancelation, the flux swing in the magnetic core is reduced, which in turn results in a smaller traverse of the *B–H* curve. The quantity of loss depends on the *B–H* curve and the material properties of the IM core. An iron-powder core material is used in this article and the coupling factor is optimized based on the core property.

It should be noted that the effect of coupling on the DMCR efficiency is twofold. First, the ac flux density swing, associated with the Steinmetz loss component [29], is reduced through flux cancelation. Second, the high-frequency current resistance, which is directly proportional to the current ripple, diminishes as well. The impact of the IM coupling on these losses is shown in Fig. 7 for a half-a-line cycle.

III. Design of the IM

To realize different coupling factors and flexibility in manipulating the flux paths, an EE core geometry is chosen for the IM. EE core is doubly stacked to increase the effective core area. Furthermore, a doubly stacked core is capable of handling higher energy, which in turn results in higher power density. To achieve a flexible coupling factor, the source-side winding of the IM is distributed on the left and middle limbs and the load-side winding is distributed on the middle and right limbs. One variation is illustrated in Fig. 8(a). The percentage of the overall inductance in each one of these coils is the main design control for the coupling factor and flux attenuation/amplification. Iron-powder material (Kool μ) from Magnetic, Inc., with a high dc-bias threshold, is chosen as the base material for the core to avoid saturation.

The interactions among the fluxes generated by each coil and winding are shown in Fig. 8(b) in the terms of their respective coupling factors. The direction of the generated flux in each coil within the structure can be either the same (blue arrow) or in the opposite (red arrow), as depicted in Fig. 8(b). Symbols $k_{12}\,(=k_{21})$, $k_{13}\,(=k_{31})$, $k_{14}\,(=k_{41})$, $k_{23}\,(=k_{32})$, $k_{24}\,(=k_{42})$,

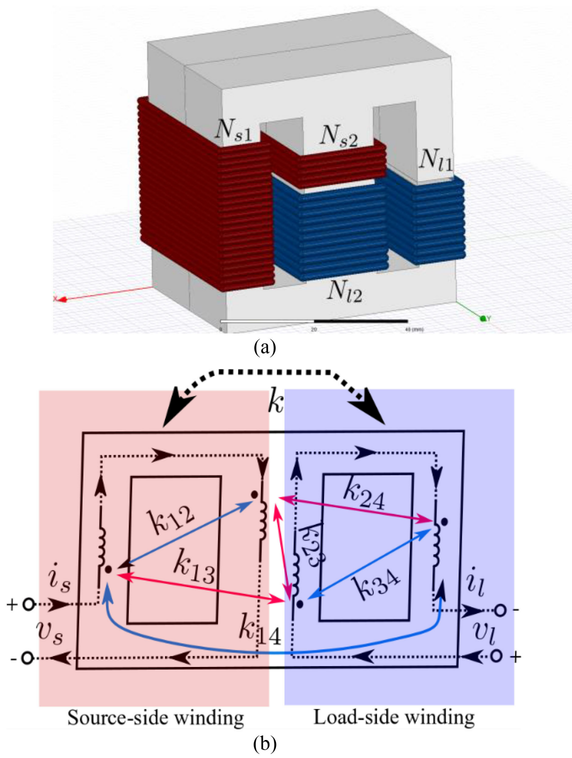

Fig. 8. (a) Layout and (b) couplings of the IM windings. (a) Location of the source- and load-side coils on the core. $\boldsymbol{N_{s1}}$ and $\boldsymbol{N_{s2}}$ are the number of turns of the source-side winding (marked in red) placed on the left and middle limbs, respectively, and $\boldsymbol{N_{l1}}$ and $\boldsymbol{N_{l2}}$ are the number of turns of the load-side winding placed on the right and middle limbs (marked in blue), respectively. (b) Couplings within and between the source- and load-side windings.

and k_{34} $(=k_{43})$ represent the couplings between $\{N_{s1}, N_{s2}\}$, $\{N_{s1}, N_{l2}\}$, $\{N_{s1}, N_{l1}\}$, $\{N_{s2}, N_{l2}\}$, $\{N_{s2}, N_{l1}\}$, and $\{N_{l1}, N_{l2}\}$, respectively. k_{11}, k_{22}, k_{33}, and k_{44} are the diagonal entries on the coupling matrices and refer to the coupling of each coil to its own flux.

To achieve high efficiency, high-power density, and desired coupling in the IM, four winding-distribution configurations [following the generic configuration in Fig. 8(a)] are considered for IM. Using the magnetostatic analysis tool available in ANSYS' Maxwell, coupling factors between the coils are simulated and captured in matrices [30] $\mathrm{k}_{\mathrm{fem}}^{(\mathrm{a})}$–$\mathrm{k}_{\mathrm{fem}}^{(\mathrm{d})}$

$$\mathrm{k}_{\mathrm{fem}}^{(\mathrm{a})} = \begin{bmatrix} 1 & 0.513 & -0.517 & -0.160 \\ 0.513 & 1 & -0.869 & -0.520 \\ -0.517 & -0.869 & 1 & 0.486 \\ -0.160 & -0.520 & 0.486 & 1 \end{bmatrix}$$

$$\mathrm{k}_{\mathrm{fem}}^{(\mathrm{b})} = \begin{bmatrix} 1 & 0.531 & -0.537 & 0.163 \\ 0.531 & 1 & -0.988 & -0.531 \\ -0.537 & -0.988 & 1 & 0.537 \\ 0.163 & -0.850 & 0.537 & 1 \end{bmatrix}$$

$$\mathrm{k}_{\mathrm{fem}}^{(\mathrm{c})} = \begin{bmatrix} 1 & 0 & 0 & -0.155 \\ 0 & 0 & 0 & 0 \\ 0 & 0 & 0 & 0 \\ -0.155 & 0 & 0 & 1 \end{bmatrix}$$

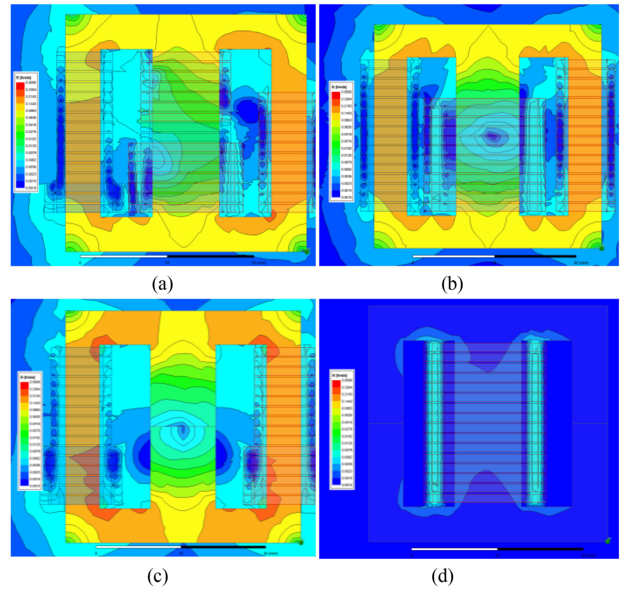

Fig. 9. CAD representation of the four winding distributions, as detailed in Table I, and their corresponding flux densities.

TABLE I
COMPARISON OF THE FOUR WINDING CONFIGURATIONS FOR THE IM DESIGN IN MAXWELL

Winding configuration	(a)	(b)	(c)	(d)
Coupling factor (k)	-0.507	-0.592	-0.155	-0.855
Winding Area [(1)] (mm^2)	98.63	102.4	56.36	81.98
Winding Weight [(2)] (g)	142.59	147.92	110.38	90.19
N_{s1}	19	16	22	0
N_{s2}	9	12	0	16
N_{l1}	12	16	22	0
N_{l2}	14	12	0	16
R_{dc} [(3)] (mΩ)	186.9	193.8	144.6	118.2
R_{ac} [(3)] (Ω)	1.09	1.13	0.84	0.69

[(1)]Calculated bare wire area.
[(2)]Weight of the bare copper.
[(3)]Collective resistance of all coils in the configuration.

$$\mathrm{k}_{\mathrm{fem}}^{(\mathrm{d})} = \begin{bmatrix} 0 & 0 & 0 & 0 \\ 0 & 1 & -0.855 & 0 \\ 0 & -0.855 & 1 & 0 \\ 0 & 0 & 0 & 0 \end{bmatrix}.$$

Furthermore, these four winding configurations of the IM are simulated and compared in flux density and overall coupling factor among the other parameters in Fig. 9 and Table I. It should be noted that the presented values in Table I are calculated, and the experimental values reflect these numbers closely and presented in Section IV.

Table I presents that the coupling requirement for ripple reduction is achieved with winding distribution instead of airgap implementation. Furthermore, a wide range of coupling factors can be achieved with relatively low impact on the losses (dc and ac resistance) and size (winding weight and area).

The winding distribution in this section is designed to envelope three general cases. First, the coupling of about -0.5 as per analysis in Section II is desired for best performance. The

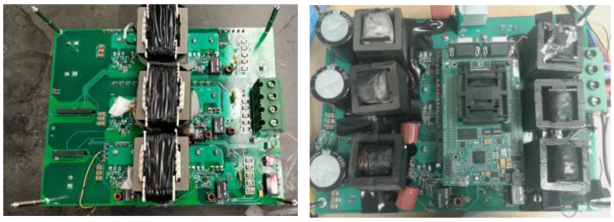

(a) (b)

Fig. 10. (a) IM- and (b) DM-based power-board designs for the DMCR. The IM-based DMCR has only three coupled inductors, while the latter has six discrete inductors.

TABLE II
EXPERIMENTAL SPECIFICATION OF BOTH IM-BASED AND DM-BASED BOARDS

Specifications	Value
Power	1 kW
Input Voltage (3Ph, RMS)	120 V
Switching Frequency	100 kHz
Input Capacitance ($C_{x,I}^{(1)}$)	4 μF
Output Capacitance ($C_{x,O}^{(1)}$)	3 mF
Blocking Capacitance ($C_{x,B}^{(1)}$)	1.5 μF

(1) Refer to Fig. (5) for the symbol in the circuit.

TABLE III
CORE SPECIFICATIONS FOR THE EXPERIMENTAL DM AND IM

Specifications	DM	IM
Part number	K4022E060	K5528E060
Material class	Koolμ(1)	Koolμ(1)
Permeability	60	60
Weight (g)	65/E	127.7/E
Cross section (mm^2)	237	350
Window Area (mm^2)	276	380

Total of six and three such DM and IM devices are required for the DM- and IM-based DMCRs.
(1) Manufactured by Magnetics, Inc.

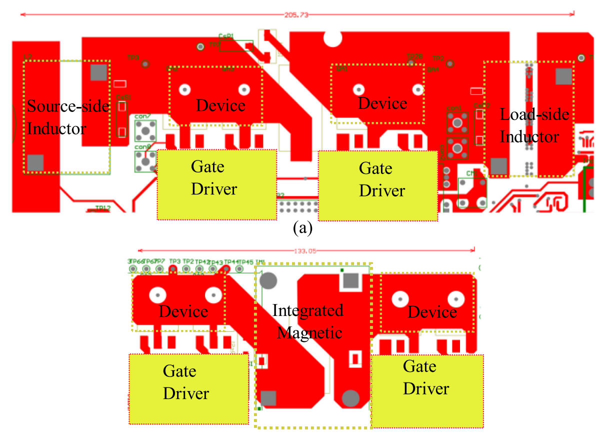

Fig. 11. Printed circuit board layouts and footprints of (a) DM- and (b) IM-based DMCR boards.

configurations in Fig. 9(a) and (b) both give ~ -0.5 with different winding placements. Second, the high coupling is aimed for winding with both coils on the middle limb. It is achieved in the configuration in Fig. 9(d) with a coupling of -0.855. Finally, the low coupling is designed on the same core by putting the coils on the far sides of the core. This gives the coupling of -0.155. All the couplings are desired to be negative to achieve ripple reduction in the DMCR. The experimental measurements and testing in the DMCR are presented in Section IV for all configurations and closely correlate to these values.

Between two different winding placements of configurations in Fig. 9(a) and (b), the asymmetric implementation of the configuration in Fig. 9(a) is preferred and chosen to be compared with DM-based DMCR. According to Table I, same inductance is achieved in configuration (a) with lower resistance, copper weight, winding area. Also, considering the field around the core, the magnetic field is more contained inside the core in the configuration in Fig. 9(a) as opposed to that in Fig. 9(b), where the higher portion of the inductance is one of the side limbs.

IV. EXPERIMENTAL REALIZATION AND RESULTS

To experimentally validate the proposed IM for the three-phase DMCR, two power-board designs based solely on IM and DM are carried out (see Fig. 10). In the IM-based design, the source- and load-side inductors of a DMCR module, as shown in Fig. 1, are coupled, while for the DM-based design, these inductors are discrete and have no coupling. All other power-stage parameters besides these differences remain the same for both the boards, as given in Table II. The core details for IM and DM are tabulated in Table III. The control approach for the DMCR is described in [24] and is the same for all magnetic and power-board variations.

A. Discrete Versus IM

As outlined in Section III, the aim of the proposed IM design is to implement ripple reduction while maintaining the current control stability, enhancing power quality, and efficiency. The purpose of the experimental boards is to enable the validation and comparison of the electrical performances of the magnetic devices. Using these IM and DM devices, two DMCR boards, as indicated earlier, are fabricated, as shown in Fig. 10.

In that regard, and to begin with, it is shown in Fig. 11 that the length of the high-frequency layout length for the IM-based DMCR board is 133 mm, while that of the DM-based DMCR board is 203 mm. The 70 mm reduction in the width with a 2 oz four-layer copper board where the forward and return paths are separated with FR4 will result in 51.5 nH and 3.3 mΩ reductions in parasitic inductance and resistance. Furthermore, the footprint of the IM-based board is reduced as well as given that the core volume of the DM is about twice that of the IM.

IM is compared with DM for one of the phases of DMCR in Fig. 12(a). The coil terminal locations and flux directions for winding configuration (a) is shown in Fig. 12(b). Flux cancelation is implemented in the middle limb. Furthermore, enough leakage is provided between the two coupled inductors to reduce the current ripple and achieve a reasonable tradeoff in size and efficiency.

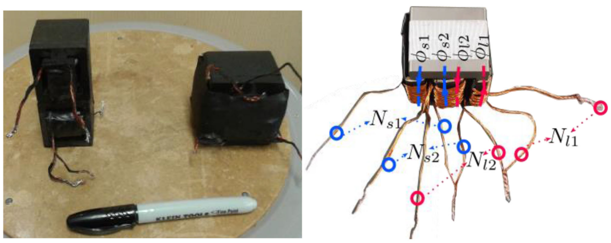

(a) (b)

Fig. 12. (a) Experimental DM and IM realizations. (b) Experimental winding configuration for the IM before isolation and coating.

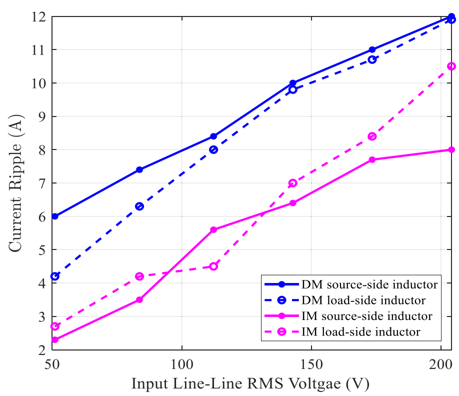

Fig. 13. Ripple current comparisons of the IM- and DM-based DMCR.

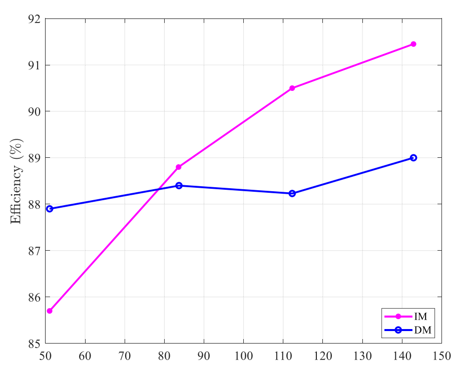

Fig. 14. Efficiency comparison of the IM- and DM-based DMCR.

The parametric comparison of the IM with the DM in these key aspects is demonstrated in Figs. 13–16. Current ripples of the source- and load-side discrete and coupled inductors of the DMCR are compared for the IM- and the DM-based designs in Fig. 13. For the IM-based DMCR, the ripple currents of the coupled inductors are reduced by approximately 30%.

In Fig. 14, efficiencies of the IM- and DM-based DMCRs are compared with variation in the input rms voltage. For this experiment, the input current of a DMCR is controlled at a peak value of 8 A. At lower voltages, when the core loss is small, the DM yields better efficiency. However, beyond ∼40% of the nominal output power (corresponding to over 60% of the nominal input voltage for a finite load), the IM-based DMCR yields higher efficiency. The overall efficiency of the DMCR is higher using the IM since the IM, compared with the DM-based DMCR, yields lower loss at higher voltages where, for the unity-power-factor DMCR, the instantaneous output power is higher as well. This is the tradeoff in the IM and DM designs that was indicated in Section III.

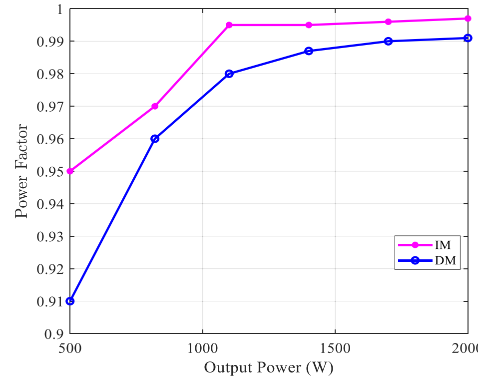

Fig. 15. Power factor of the IM- and DM-based DMCR.

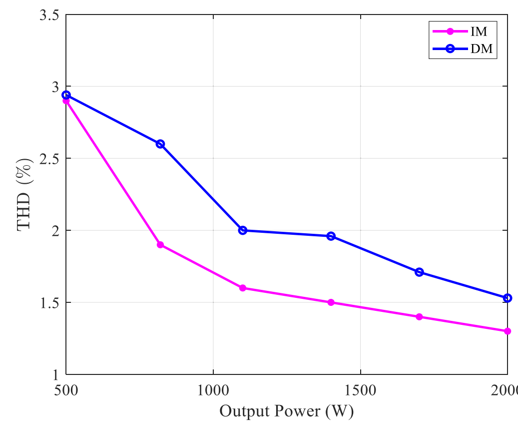

Fig. 16. Input-current THDs of the IM- and DM-based DMCRs.

Next, the impact of IM on the power quality of the ac input of the DMCR is explored. Fig. 15 demonstrates the input power factor of the DMCR with varying output power for the IM- and DM-based DMCRs, demonstrating an improved performance for the former. In Fig. 16, the input-current THDs of the DMCRs using the IM- and DM-based designs are provided. For a wide range of output power, the IM-based design provides a tangible reduction in low-frequency harmonic distortion.

In Fig. 17, using the time-domain experimental results, the performance and stability of the IM- and DM-based experimental DMCR prototypes are demonstrated. It is apparent from the two sets of waveforms that while both the designs are inherently stable at the 60-Hz time scale, the IM-based design yields reduced input-current distortions.

B. IM With Varying Winding Configurations (Coupling Factors)

Four winding configurations formerly introduced in Section III are experimentally fabricated and tested on the IM-based DMCR board. Core specifications in all cases are provided in Table III. In Fig. 18(a)–(d), four different IM configurations are

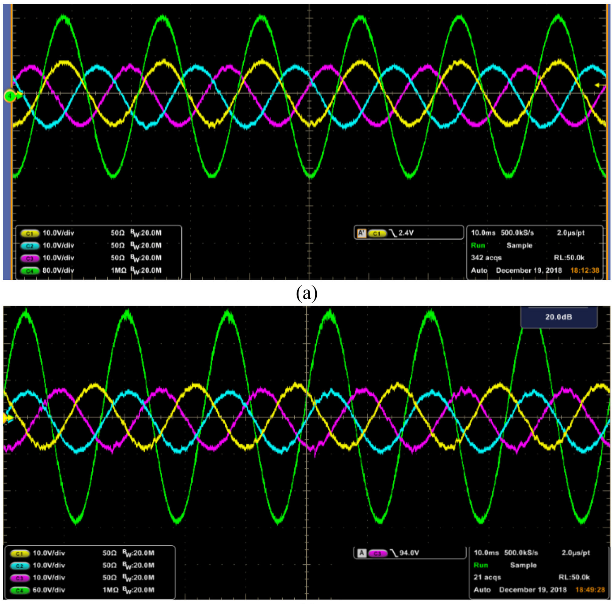

Fig. 17. Time-domain experimental results of (a) IM- and (b) DM-based DMCRs with controlled 8 A input peak current. Blue, yellow, and purple traces in (a) and (b) phase-A current (10 A/div), phase-B current (10 A/div), and phase-C current (10 A/div). Green trace: line-neutral voltage at 80 V/div in (a) and at 60 V/div in (b).

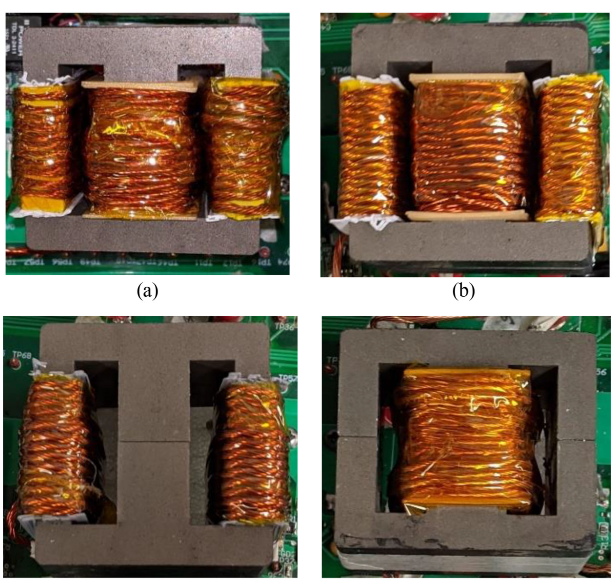

Fig. 18. Fabricated IM for the DMCR in different winding configurations to achieve various coupling factors (a)–(d) corresponding to Fig. 9(a)–(d).

presented. The experimental inductances are measured with an HP 4192A LF impedance analyzer and presented in Table IV. The coupling matrices of each configuration are measured for all the coils on the core and are as follows:

$$k_{\mathrm{exp}}^{(a)} = \begin{bmatrix} 1 & 0.480 & -0.477 & -0.132 \\ 0.480 & 1 & -0.873 & -0.876 \\ -0.477 & -0.873 & 1 & 0.455 \\ -0.132 & -0.876 & 0.455 & 1 \end{bmatrix}$$

TABLE IV
MEASURED INDUCTANCE AND RESISTANCE OF CONFIGURATIONS, AS SHOWN IN Fig. 9(a)–(d)

Winding configuration	(a)	(b)	(c)	(d)
Coupling factor (k)	-0.507	-0.592	-0.155	-0.855
L_s (µH)	113.28	168.8	110.2	97.96
L_p (µH)	116.84	153.3	117.8	107.78
L_m(µH)	-64.75	-97.92	-16.15	-83.81
R_{dc} (1) (mΩ)	171	110.5	78.5	80.2
R_{ac} (1) (Ω)	1.38	1.58	1.37	1.63

(1) Collective resistance of all coils in the configuration.

$$k_{\mathrm{exp}}^{(b)} = \begin{bmatrix} 1 & 0.478 & -0.486 & 0.144 \\ 0.478 & 1 & -0.964 & -0.461 \\ -0.486 & -0.964 & 1 & 0.471 \\ 0.144 & -0.461 & 0.471 & 1 \end{bmatrix}$$

$$k_{\mathrm{exp}}^{(c)} = \begin{bmatrix} 1 & 0 & 0 & -0.141 \\ 0 & 0 & 0 & 0 \\ 0 & 0 & 0 & 0 \\ -0.141 & 0 & 0 & 1 \end{bmatrix}$$

$$k_{\mathrm{exp}}^{(d)} = \begin{bmatrix} 0 & 0 & 0 & 0 \\ 0 & 1 & -0.815 & 0 \\ 0 & -0.815 & 1 & 0 \\ 0 & 0 & 0 & 0 \end{bmatrix}.$$

These coupling matrices experimentally measured ($k_{\mathrm{exp}}^{(a)} - k_{\mathrm{exp}}^{(d)}$) are closely following the finite-element prediction in Section III ($k_{\mathrm{fem}}^{(a)} - k_{\mathrm{fem}}^{(d)}$).

As explained in Section III, due to amplified flux coupling between the coils of the same inductor (see Fig. 8, blue arrows), the inductances are highest for configurations, as shown in Fig. 9, with higher couplings among those coils. Consequently, the configuration in Fig. 9(a) will result in a lower inductance compared with that Fig. 9(b), although they have approximately the same coupling factor between the load- and source-side windings. The latter will result in higher THD but reduced losses.

To experimentally validate the effect of the IM coupling on the performance parameters of the DMCR, as explained in computational results and analyses in Section II, winding configurations, as shown in Fig. 9(a)–(d), are subsequently implemented on the same core (K5528E060), as shown in Fig. 18(a)–(b). In this section, the time-domain performance, THD, losses, and thermal performance of these configurations are explored. All tests in this section are conducted on the IM-based board, as shown in Fig. 10(a). The four winding configurations alluded to above are compared regarding their coupling factors. The control architecture and compensation gains are kept unchanged while comparing all of these four cases.

The time-domain three-phase currents are shown for the fur winding configurations, as shown in Fig. 19(a). The peak current is controlled at 4 A with an input voltage of 120 V rms in all configurations (1 kW). The time-domain performance of the DMCR is consistent in all cases.

The frequency decomposition of the input line current of the DMCR is shown in Fig. 19(b). It demonstrates that the amplitudes of the input-line-current harmonics increase with

TABLE V
EXPERIMENTAL AND PREDICTED LOSS BREAKDOWN OF THE DMCR FOR THE FOUR WINDING CONFIGURATIONS OF THE IM

	Winding Configurations							
	(a)		(b)		(c)		(d)	
	Predicted	Experimental	Predicted	Experimental	Predicted	Experimental	Predicted	Experimental
Coupling	-0.507	-0.5628	-0.592	-0.6074	-0.155	-0.1417	-0.855	-0.8153
Dc Copper (W)	4.89	4.07	5.34	3.34	3.33	3.30	3.40	2.77
Ac Copper (W)	24.05	35.12	15.07	31.21	40.78	59.24	27.47	30.86
Core (W)	3.22	-	1.40	-	7.28	-	0.507	-
Conduction (W)	6.53	-	5.42	-	8.43	-	6.4	-
Switching (W)	40.06	-	40.24	-	39.75	-	40.18	-
Total (W)	78.75	81.30	67.47	80.05	99.48	92.86	77.95	80.03

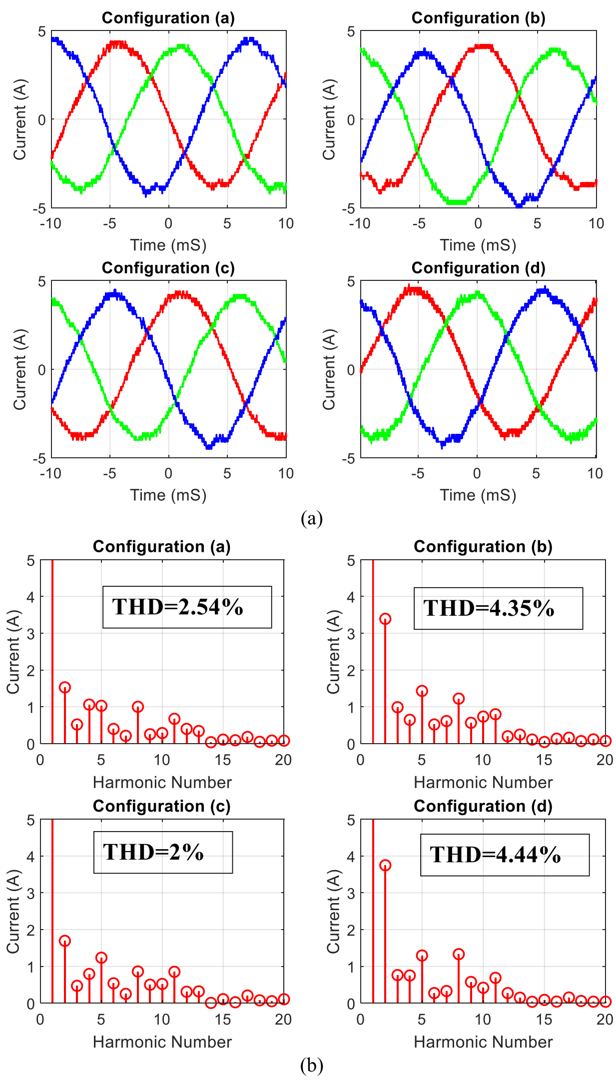

Fig. 19. Comparison of the time- and frequency-domain performances of the four experimentally realized winding configurations of the IM. The results are obtained using a TPS 2024B oscilloscope from Tektronix.

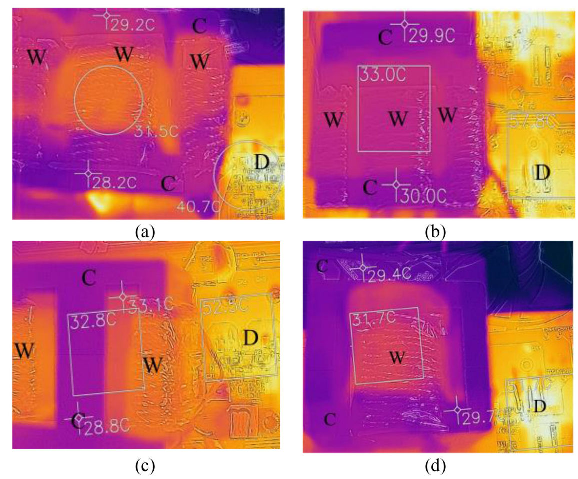

Fig. 20. Thermal performances of the IM for the four winding configurations. The windings are annotated as "W," magnetic cores as "C," and device as "D."

higher coupling factors, which matches the predictions of the analyses and simulations, as conducted in Section II.

The thermal images of the cores and windings of the IM are shown in Fig. 20 in the IR format taken by FLIR one thermal camera. The thermal images of the IM are captured along with the thermal images of the SiC-MOSFET C2M0080120D to provide a relative comparison. A natural-conduction cooling is adopted for both the SiC MOSFET and the IM. The thermal performances of all the windings for the four IM configurations are found to be similar. For the four IM winding configurations, the core temperature rise for the IMs (as captured in Fig. 20) is found to be 4.2 °C, 4.9 °C, 7.8 °C, and 4.4 °C and the winding temperature rise is 6.5 °C, 8 °C, 11.8 °C, and 6.7 °C, respectively, above an ambient room temperature of 25 °C. This increase in the temperatures of the four IM parts is primarily attributed to their copper and core losses, as captured in Table V.

The loss breakdowns of the IM in DMCR for all of the four winding configurations of the IM are presented in Table V. These data are compared with the experimental losses at 1 kW for all configurations. The switching loss is calculated following the method, as presented in [31], based on the charge-equivalent approximation of the SiC-MOSFET capacitances relying solely on the datasheet parameters. The conduction loss is calculated based on the measured rms current through the source-side and load-side inductors. The winding ac and dc resistances are measured following the algorithm outlined in [32]. The magnetic core losses are calculated based on the reluctance model of the IM winding configuration and fitting the material curves given in the manufacturer's datasheet [33].

As stated earlier, the magnetic losses (core and ac copper) are the lowest in the configuration in Fig. 19(d) (that has the highest coupling factor), while it is the highest in the configuration in Fig. 19(c) (that has the lowest coupling factor). The experimental results show a close correlation with the design prediction.

However, as given in Table V, the other components of the IM loss are also affected by changing the winding configuration (that affects their coupling factors). It is noted that the copper losses follow the winding configurations and ultimately will affect the overall losses. The lowest coupling yields the highest copper loss captured by the brighter thermal image, as indicated in Fig. 20. Since the ripple current increases with a lower coupling factor, the ac copper loss for such an IM configuration increases as well. The device losses are closely matched in all cases so that the difference in the experimental results is caused by changes in core and ac copper losses due to the coupling variations. On the other hand, as shown in Fig. 19, the THD is adversely affected at higher couplings. It should be noted in all configurations that the ripple cancelation is done to some extent.

V. Conclusion

In this article, the realizability and validation of an IM design for a three-phase DMCR have been presented. The IM has been optimized after pursuing several winding-distribution scenarios and simulated using circuit and finite-element-analysis tools. Subsequently, its performance and efficacy have been validated using experimentally realized and tested prototypes at the component and converter levels. It has been shown that, for the symmetric DMCR topology, the coupling factor of the IM can be modulated to yield reduction in aggregate loss and size of the IM (compared with the DM) devices aside from providing an acceptable THD and ensuring converter stability. The outlined IM has the potential for high-efficiency and high-power density applications.

Acknowledgment

The views and opinions of the authors expressed herein do not necessarily state or reflect those of the United States Government or any agency thereof.

References

[1] G. B. Crouse, “Electrical filter,” U.S. Patent 1 920 948, Aug. 1, 1933.
[2] J. R. Cielo and H. S. Hoffman, “Combined transformer and inductor device,” U.S. Patent 3 694 726, Sep. 1972.
[3] S. Cuk, “A new zero-ripple switching dc-to-dc converter and integrated magnetics,” *IEEE Trans. Magn.*, vol. 19, no. 2, pp. 57–75, Mar. 1983.
[4] R. J. Kaplar, J. C. Neely, D. L. Huber, and L. J. Rashkin, “Generation-after-next power electronics: Ultrawide-bandgap devices, high-temperature packaging, and magnetic nanocomposite materials,” *IEEE Power Electron. Mag.*, vol. 4, no. 1, pp. 36–42, Mar. 2017.
[5] J. Rąbkowski, D. Peftitsis, and H.-P. Nee, “Silicon carbide power transistors: A new era in power electronics is initiated,” *IEEE Ind. Electron. Mag.*, vol. 6, no. 2, pp. 17–26, Jun. 2012.
[6] I. D. Jitaru and A. Ivascu, “Quasi-integrated magnetic: An avenue for higher power density and efficiency in power converters,” in *Proc. Appl. Power Electron. Conf.*, 1997, pp. 395–402.
[7] K. Shenai, P. G. Neudeck, and G. Schwarze, “Design and technology of compact high-power converters,” *IEEE Aerosp. Electron. Syst. Mag.*, vol. 16, no. 3, pp. 27–31, Mar. 2001.
[8] A. Bindra and T. Keim, “Exciting advances in power electronics,” *IEEE Power Electron. Mag.*, vol. 5, no. 2, pp. 49–55, Jun. 2018.
[9] A. J. Hanson, J. A. Belk, S. Lim, C. R. Sullivan, and D. J. Perreault, “Measurements and performance factor comparisons of magnetic materials at high frequency,” *IEEE Trans. Power Electron.*, vol. 31, no. 11, pp. 7909–7925, Nov. 2016.
[10] C.-T. Pan, M.-C. Cheng, and C.-M. Lai, “A novel integrated dc/ac converter with high voltage gain capability for distributed energy resource systems,” *IEEE Trans. Power Electron.*, vol. 27, no. 5, pp. 2385–2395, May 2012.
[11] D. Pan, X. Ruan, C. Bao, W. Li, and X. Wang, “Magnetic integration of the LCL filter in grid-connected inverters,” *IEEE Trans. Power Electron.*, vol. 29, no. 4, pp. 1573–1578, Apr. 2014.
[12] G. Gohil, L. Bede, R. Teodorescu, T. Kerekes, and F. Blaabjerg, “An integrated inductor for parallel interleaved three-phase voltage source converters,” *IEEE Trans. Power Electron.*, vol. 31, no. 5, pp. 3400–3414, May 2016.
[13] M. Das and V. Agarwal, “Generalized small signal modeling of coupled-inductor-based high-gain high-efficiency dc-dc converters,” *IEEE Trans. Ind. Appl.*, vol. 53, no. 3, pp. 2257–2270, May/Jun. 2017.
[14] M. Forouzesh, Y. P. Siwakoti, F. Blaabjerg, and S. Hasanpour, “Small-signal modeling and comprehensive analysis of magnetically coupled impedance-source converters,” *IEEE Trans. Power Electron.*, vol. 31, no. 11, pp. 7621–7641, Nov. 2016.
[15] A. A. Khan, H. Cha, and H.-G. Kim, “Magnetic integration of discrete-coupled inductors in single-phase direct PWM AC-AC converters,” *IEEE Trans. Power Electron.*, vol. 31, no. 3, pp. 2129–2138, Mar. 2016.
[16] H. Liu and D. Zhang, “Two-phase interleaved inverse-coupled inductor boost without right half-plane zeros,” *IEEE Trans. Power Electron.*, vol. 32, no. 3, pp. 1844–1859, Mar. 2017.
[17] J. Imaoka *et al.*, “A magnetic design method considering dc-biased magnetization for integrated magnetic components used in multiphase boost converters,” *IEEE Trans. Power Electron.*, vol. 33, no. 4, pp. 3346–3362, Apr. 2018.
[18] M. Wu, S. Li, S.-C. Tan, and S. Y. Hui, “Optimal design of integrated magnetics for differential rectifiers and inverters,” *IEEE Trans. Power Electron.*, vol. 33, no. 6, pp. 4616–4626, Jun. 2018.
[19] B. Zaidi, A. Videt, and N. Idir, “Optimization method of CM inductor volume taking into account the magnetic core saturation issues,” *IEEE Trans. Power Electron.*, vol. 34, no. 5, pp. 4279–4291, May 2019.
[20] S. Zhao, Q. Li, F. C. Lee, and B. Li, “High-frequency transformer design for modular power conversion from medium-voltage ac to 400 V dc,” *IEEE Trans. Power Electron.*, vol. 33, no. 9, pp. 7545–7557, Sep. 2018.
[21] V. Vorpérian, “The effect of the magnetizing inductance on the small-signal dynamics of the isolated Ĉuk converter,” *IEEE Trans. Aerosp. Electron. Syst.*, vol. 32, no. 3, pp. 967–983, Jul. 1996.
[22] G. Zhu, B. A. McDonald, and K. Wang, “Modeling and analysis of coupled inductors in power converters,” *IEEE Trans. Power Electron.*, vol. 26, no. 5, pp. 1355–1363, May 2011.
[23] D. K.-W. Cheng, L.-P. Wong, and Y.-S. Lee, “Design, modeling, and analysis of integrated magnetics for power converters,” in *Proc. IEEE 31st Power Electron. Spec. Conf.*, 2000, pp. 320–325.
[24] N. Kumar, S. K. Mazumder, and A. Gupta, “SiC dc fast charger control for electric vehicles,” in *Proc. IEEE Energy Convers. Congr. Expo.*, 2018, pp. 599–605.
[25] S. Mehrnami, S. K. Mazumder, and H. Soni, “Modulation scheme for three-phase differential-mode Ĉod inverter,” *IEEE Trans. Power Electron.*, vol. 31, no. 3, pp. 2654–2668, Mar. 2016.
[26] N. Kumar, M. Mohamadi, and S. K. Mazumder, “Passive damping optimization of the integrated-magnetics based differential-mode-Cuk-rectifier,” *IEEE Trans. Power Electron.*, vol. 35, no. 10, pp. 10008–10012, Oct. 2020.
[27] J. Wang, K. J. Dagan, X. Yuan, W. Wang, and P. H. Mellor, “A practical approach for core loss estimation of a high-current gapped inductor in PWM converters with a user-friendly loss map,” *IEEE Trans. Power Electron.*, vol. 34, no. 6, pp. 5697–5710, Jun. 2019.
[28] J. Mühlethaler, J. Biela, J. W. Kolar, and A. Ecklebe, “Core losses under the dc bias condition based on Steinmetz parameters,” *IEEE Trans. Power Electron.*, vol. 27, no. 2, pp. 953–963, Feb. 2012.
[29] W. T. McLyman, *Designing Magnetic Components for High Frequency Dc-Dc Converters*. Idyllwild, CA, USA: Kg Magnetics, 1993.
[30] Z. Zhang, “Coupled-inductor magnetics in power electronics,” Ph.D. dissertation, Dept. Eng. Appl. Sci., California Inst. Technol., Pasadena, CA, USA, 1987.
[31] D. Christen and J. Biela, “Analytical switching loss modeling based on datasheet parameters for mosfets in a half-bridge,” *IEEE Trans. Power Electron.*, vol. 34, no. 4, pp. 3700–3710, Apr. 2019.
[32] B. X. Foo, A. L. F. Stein, and C. R. Sullivan, “A step-by-step guide to extracting winding resistance from an impedance measurement,” in *Proc. IEEE Appl. Power Electron. Conf. Expo.*, Tampa, FL, USA, 2017, pp. 861–867.
[33] Magnetic Powder Core Cataloge, 2020. [Online]. Available: https://www.mag-inc.com/Design/Technical-Documents/Powder-Core-Documents.html

Moien Mohamadi (Student Member, IEEE) received the M.Sc. degree in electrical engineering from the Isfahan University of Technology, Isfahan, Iran, in 2017. He is currently working toward the Ph.D. degree with the Laboratory for Energy and Switching-Electronics Systems, University of Illinois at Chicago, Chicago, IL, USA.

Since 2014, he has been working in power electronics research and development and a member of the PES community. He is currently involved in the research of highly efficient and compact fast battery charger. His research interests include optimal design and hardware realization of highly efficient and compact power electronics converter, high-frequency magnetic design, optimization, and hardware realization, and soft-switching power electronics.

Sudip Kumar Mazumder (Fellow, IEEE) received the M.S. degree in electrical power engineering from Rensselaer Polytechnic Institute, Troy, NY, USA, in 1993, and the Ph.D. degree in electrical and computer engineering from Virginia Tech, Blacksburg, VA, USA, in 2001.

He has been a Professor with the University of Illinois at Chicago (UIC), Chicago, IL, USA, since 2001, and the President of Next Watt LLC, Chicago, IL, USA, since 2008. He has around 30 years of professional experience and has held R&D and design positions in leading industrial organizations and has served as a Technical Consultant for several industries. He has developed novel multiscale methodologies for controlling power-electronic systems and networks at wide-/narrow-bandgap semiconductor device level resulting in a plurality of practical applications. He has also made multiple novel contributions to the areas of high-frequency-link power electronics, including hybrid modulation and differential-mode-converter topology, and optically-controlled power semiconductor devices and power electronics.

Dr. Mazumder was a recipient of several IEEE awards, including the Prize Paper Award from the IEEE TRANSACTIONS ON POWER AND ELECTRONICS and IEEE International Future Energy Challenge Award, the U.S. National Science Foundation CAREER Award in 2003, the U.S. Office of Naval Research Young Investigator Award in 2005; at UIC, University Scholar Award—the highest award of the university in 2013, Inventor of the Year Award in 2014, and the Distinguished Researcher Award in Natural Sciences and Engineering in 2020. He was named a fellow of the American Association for the Advancement of Science in 2020 for distinguished contributions to the field of multiscale control and analysis of power-electronic systems. From 2016 to 2019, he was a Distinguished Lecturer for IEEE PELS and currently serves as a Regional Distinguished Lecturer for the U.S. region. He currently serves as the Editor-in-Chief at Large for the IEEE TRANSACTIONS OF POWER ELECTRONICS and the leading journal in *Power Electronics*. He was an Administrative Committee Member and a Member-at-Large for IEEE PELS in 2015 and 2020, respectively, and the Chair for the IEEE PELS Technical Committee on Sustainable Energy Systems from 2015 to 2020.

Nikhil Kumar (Student Member, IEEE) received the B.E. degree in electrical engineering in 2011 from the Delhi College of Engineering, Delhi, India, and the M.S. degree in electrical engineering in 2015 from the University of Illinois at Chicago, Chicago, IL, USA, where he is currently working toward the Ph.D. degree with the Department of Electrical and Computer Engineering.

His research interests focus on the analysis and design of wide-band-gap device-based high-power electronics converters for dc fast charging and microinverter applications.

Mr. Kumar serves as a reviewer for the IEEE TRANSACTIONS ON POWER ELECTRONICS and IEEE TRANSACTIONS ON INDUSTRIAL ELECTRONICS.